Synthesis and Thermoelectric Properties of Zr$_x$Ti$_{1-x}$NiSn$_{0.98}$Sb$_{0.02}$ n-Type Half-Heusler Materials

Sung-Jae Joo[1] · Ji-Hee Son[1] · Ho Seong Lee[2] · Jeongin Jang[1] · Bong-Seo Kim[1] · Bok-Ki Min[1]

Abstract

Hf-free Zr$_x$Ti$_{1-x}$NiSn$_{0.98}$Sb$_{0.02}$ ($x = 0.25$, 0.5, 0.75) n-type half-Heusler (HH) thermoelectric materials were synthesized by a serial processing method including induction melting (IM), annealing, ball milling, and spark plasma sintering (SPS). For comparison, a Hf-containing half-Heusler Hf$_{0.25}$Zr$_{0.25}$Ti$_{0.5}$NiSn$_{0.98}$Sb$_{0.02}$ ingot was also alloyed by arc melting, and the effects of Hf on the thermoelectric properties were estimated. The Zr$_x$Ti$_{1-x}$NiSn$_{0.98}$Sb$_{0.02}$ HH materials were nearly pure according to the x-ray diffraction analysis, but microscopic investigation revealed impurity phase inclusions of unalloyed Sn, Zr, and Ti. The power factor (PF) of the Hf-free HH materials reached the maximum value of 4.31 mWm^{-1} K^{-2} at 823 K in Zr$_{0.75}$Ti$_{0.25}$NiSn$_{0.98}$Sb$_{0.02}$, which was higher than Hf$_{0.25}$Zr$_{0.25}$Ti$_{0.5}$NiSn$_{0.98}$Sb$_{0.02}$ (4.01 mWm^{-1} K^{-2} at 773 K) in this study. However, the thermal conductivity of the Hf-free samples was significantly higher, by which the maximum dimensionless figure of merit was slightly lower (ZT$_{max}$ = 0.92 in Zr$_{0.75}$Ti$_{0.25}$NiSn$_{0.98}$Sb$_{0.02}$ at 873 K) than that of Hf$_{0.25}$Zr$_{0.25}$Ti$_{0.5}$NiSn$_{0.98}$Sb$_{0.02}$ (ZT$_{max}$ = 1.03 at 873 K). The thermal conductivity was decomposed into lattice and electronic contributions, and the possible correlation with Ni off-stoichiometry is discussed.

Introduction

Climate change due to global warming has become an imminent problem requiring urgent countermeasures. Among the many green technologies, waste heat recovery by thermoelectric generation (TEG) has been regarded as a viable measure to reduce fossil fuel consumption and CO$_2$ emissions. TEG has many advantages including noiseless operation, small size, and long-term reliability,[1–3] and the conversion efficiency is quantified by the dimensionless figure of merit ZT = $\sigma S^2 T/\kappa$, where σ is the electrical conductivity, S is the Seebeck coefficient, T is the absolute temperature, and κ is the thermal conductivity.

✉ Sung-Jae Joo
sj_joo@keri.re.kr

1 Energy Conversion Research Center, Korea Electrotechnology Research Institute, Changwon 51543, Republic of Korea

2 School of Materials Science and Engineering, Kyungpook National University, 80 Daehak-ro, Buk-gu, Daegu 41566, Republic of Korea

Half-Heusler (HH) materials have attracted great attention for mid-temperature applications due to their good thermoelectric performance, mechanical strength, and thermal stability.[4–9] HH materials have a face-centered cubic structure (space group $F\bar{4}3m$) with four interpenetrating sublattices, one of which is vacant,[8,10] and independent doping in each sublattice provides additional degrees of freedom to tailor the thermoelectric properties. Among the many HH compounds, MNiSn (M = Ti, Zr, Hf) is the representative n-type material that has been widely studied,[4,11–17] and a maximum dimensionless figure of merit (ZT$_{max}$) up to 1.5 was recently attained from the best materials produced by state-of-the-art processes.[17] In the case of MNiSn compounds, isovalent alloying of Hf, Zr, and Ti at the M site is known to be very effective in lowering the lattice thermal conductivity,[12,14,16,18,19] which has been a major breakthrough for the enhancement of ZT.

However, in spite of this proven advantage, continuous attempts to reduce the amount of Hf have been made at the same time due to the scarcity and cost of Hf.[4,17,18,20] Currently, developing a synthesis process for high-performance Hf-free HH materials is one of the major goals in HH research, and a recent report has proven that ZT

values higher than 1.2 are achievable from the Hf-free $Ti_xZr_{1−x}NiSn_{0.98}Sb_{0.02}$, which were doped with Nb and V.[17]

Along with the low cost of raw materials, the simplicity and scalability of the synthesis process are also very important for industrialization. However, a majority of the previous studies on *M*NiSn employed either arc melting or levitation melting for alloying,[4–6,12,14–21] which are neither simple nor scalable for production. Therefore, in this study, we employed a conventional induction melting (IM) for the preparation of Hf-free $Zr_xTi_{1−x}NiSn_{0.98}Sb_{0.02}$ ($x = 0.25$, 0.5, 0.75) ingots, and the thermoelectric properties (TEP) were analyzed. For comparison, a Hf-containing HH ingot, $Hf_{0.25}Zr_{0.25}Ti_{0.5}NiSn_{0.98}Sb_{0.02}$, was also prepared using arc melting, and the effect of Hf isoelectronic doping on the TEP was estimated.

Experimental Procedure

Elemental source materials of Zr (99.8%, 3–6 mm lump, Alfa Aesar), Ti (99.99%, 2–10 mm grains, Kojundo), Ni (99.995%, slug 3.175 mm diameter × 3.175 mm length, Alfa Aesar), Sn (99.999%, 2–3 mm grains, Kojundo), and Sb (99.999%, ca. 2 mm grains, Kojundo) were used for synthesis of $Zr_xTi_{1−x}NiSn_{0.98}Sb_{0.02}$ ($x = 0.25$, 0.5, 0.75), and Hf (99.9%, 3–12 mm pieces, Alfa Aesar) was additionally included when $Hf_{0.25}Zr_{0.25}Ti_{0.5}NiSn_{0.98}Sb_{0.02}$ was alloyed by arc melting. These raw materials for $Zr_xTi_{1−x}NiSn_{0.98}Sb_{0.02}$ compounds were weighed according to the required stoichiometry, sealed in a quartz tube in an Ar atmosphere, loaded into a vacuum furnace, and then melted completely by radio-frequency induction heating. The melted metal was immediately quenched in water, crushed into smaller pieces, and then vacuum-sealed in a quartz tube again for long-term annealing (1173 K, 7 days). The annealed samples were then ball-milled at 300 rpm (PM-100, Retsch), and the milled powders were sieved to filter out large particles (≥ 45 μm). Finally, the sieved powders were loaded into a graphite mold (12.7 mm diameter) and spark plasma-sintered (SPS, Dr. Sinter, Fuji Electronic Industrial) at 1373 K for 10 min with a pressure of 65 MPa. The sintered ingots were sawed to various sizes using a wire saw to measure the resistivity (ρ), Seebeck coefficient (S), thermal diffusivity (a), and the heat capacity (C_p).

In the case of $Hf_{0.25}Zr_{0.25}Ti_{0.5}NiSn_{0.98}Sb_{0.02}$ synthesis, the mixed-source metals were alloyed by arc melting. During the arc melting, the samples were flipped and remelted five times on the water-cooled Cu hearth for homogenization, and the whole process after arc melting was the same as mentioned above.

The samples were analyzed by x-ray diffractometry (XRD) (CuKa, X'Pert PRO MPD, Panalytical), and the lattice parameters were estimated from the XRD patterns of the sintered powders using the Rietveld method. Field emission scanning electron microscopy (FE-SEM, Mira-II, Tescan) and field emission transmission electron microscopy (FE-TEM, Titan G2 ChemiSTEM Cs probe, FEI), each equipped with an energy-dispersive x-ray spectroscopy (EDS) apparatus, were used for microstructure investigation and element mapping. ρ and S were simultaneously measured using a commercial system (ZEM-3, Ulvac-Riko). A differential scanning calorimeter (DSC 404C, Netzsch) and a laser flash measurement system (LFA-457, Netzsch) were also used to measure C_p and a of the samples, respectively. The density (d) of the samples was measured using the Archimedes method. From these parameters, thermal conductivity κ was calculated according to the relation $\kappa = aC_pd$. The carrier concentration and mobility of the HH samples were obtained from the Hall measurement at a temperature range of 10–300 K using a physical properties measurement system (PPMS, Quantum Design).

Results and Discussions

Figure 1 shows the XRD patterns of $Zr_xTi_{1−x}NiSn_{0.98}Sb_{0.02}$ bulk samples after SPS. All major peaks are indexed according to the reference patterns of ZrNiSn (JCPDS #03-065-5987) and TiNiSn (JCPDS #00-023-1281), and traces of impurity phases are slightly visible in the range of 30°–40°. These small impurity peaks were found to indicate the
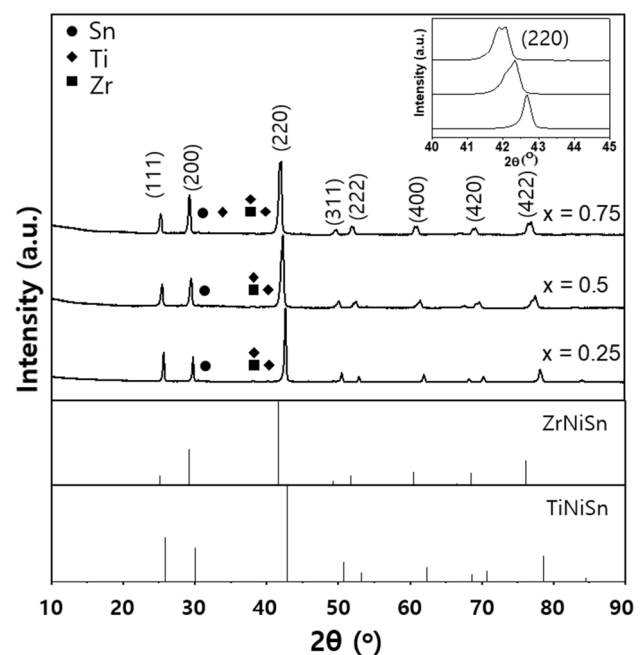

Fig. 1 X-ray diffraction patterns for the $Zr_xTi_{1−x}NiSn_{0.98}Sb_{0.02}$ samples ($x = 0.25$, 0.5, 0.75). The inset shows the magnified images of (220) peaks.

existence of unalloyed Sn, Zr, and Ti, which was confirmed by EDS analysis (Fig. 3). The inset magnifies the strongest (220) peaks shifting towards lower angles as the Zr/Ti molar ratio increases, which is due to the larger lattice parameter of ZrNiSn (6.11 Å) than that of TiNiSn (5.92Å). Table I shows the experimental average lattice parameters of our $Zr_xTi_{1-x}NiSn_{0.98}Sb_{0.02}$ bulk samples obtained from XRD analysis, but the asymmetric shapes of the (220) peaks indicate that the materials are not homogeneous with single lattice parameters. It is well known that the ZrNiSn–TiNiSn pseudo-binary system has a miscibility gap that separates the Ti-rich phase from the Ti-poor phase.[6,8,22] The phase separation was reproduced in this study, and the (220) peaks of the $Zr_xTi_{1-x}NiSn_{0.98}Sb_{0.02}$ samples ($x = 0.25, 0.5, 0.75$) were nicely decomposed into two smaller peaks, the positions of which are listed in Table I. Although the (220) peak of the $Zr_{0.25}Ti_{0.75}NiSn_{0.98}Sb_{0.02}$ sample seems almost symmetric, it also contains two peaks, and the much lower intensity of the smaller peak gives it the appearance of a single phase.

Figure 2a, b, and c show the microscopic morphology of the $Zr_xTi_{1-x}NiSn_{0.98}Sb_{0.02}$ samples observed by FE-SEM. Large-sized, round-shaped grains are mixed with small grains of a few micrometers in diameter, and among the three samples, $Zr_{0.75}Ti_{0.25}NiSn_{0.98}Sb_{0.02}$ has a higher areal ratio of the large grains. Figure 3a, b, c, d, e, and f display the representative SEM image and two-dimensional EDS element maps in the $Zr_{0.25}Ti_{0.75}NiSn_{0.98}Sb_{0.02}$ sample, which shows that impurity phases including unalloyed Zr, Sn, and Ti are present between the large grains of HH phase. The amounts of these impurity phases are slightly above the XRD detection limits. Inclusions of unalloyed Sn, Zr and Ti were found irrespective of visually complete melting during IM, and we think that optimization of the synthesis process to ensure complete alloying of the elements is additionally required. Remelting the ingots several times may eliminate the unalloyed elements. On the other hand, in the element maps of Fig. 3c and f, the uneven intensities of the spots representing Zr and Ti
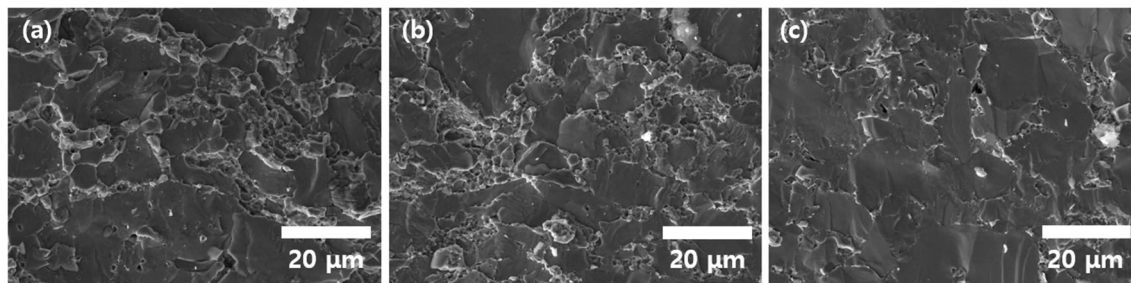

Fig. 2 SEM images of the fractured surfaces for the $Zr_xTi_{1-x}NiSn_{0.98}Sb_{0.02}$ samples: (a) $x = 0.25$, (b) $x = 0.5$, (c) $x = 0.75$.
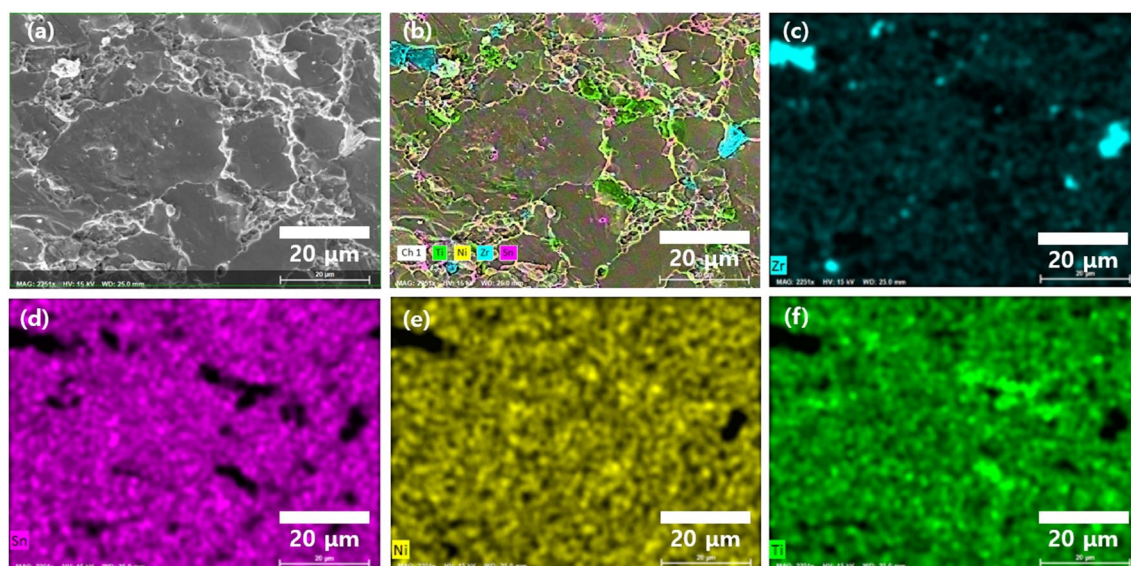

Fig. 3 (a) A SEM image of the fractured surface of the $Zr_{0.25}Ti_{0.75}NiSn_{0.98}Sb_{0.02}$ sample, (b) elemental distribution maps of Ti (green), Ni (yellow), Zr (blue), and Sn (red) superposed on the SEM image of the $Zr_{0.25}Ti_{0.75}NiSn_{0.98}Sb_{0.02}$ sample, and single element map in the same area of (c) Zr, (d) Sn, (e) Ni, and (f) Ti.

may indicate the microscale phase separation which was observed in the XRD patterns.

Figure 4a, b, c, and d are TEM images and an EDS element map of the $Zr_{0.75}Ti_{0.25}NiSn_{0.98}Sb_{0.02}$ sample. Figure 4a and b show that the microstructure of the sample is characterized by numerous dislocations at the grain boundaries as well as in the grains. In addition to dislocations, small regions of impurity phases were also identified, as shown in Fig. 4c and d. Unalloyed Zr and Ti inclusions were embedded in the matrix, which is in agreement with the XRD patterns (Fig. 1) and SEM results (Fig. 3).

The actual composition of the samples was measured using EDS at multiple spots during SEM analysis, and Table II summarizes the results. It is noted in Table II that the elements with low melting temperatures, Sn and Sb, are deficient in all samples, and Sb loss is significant, which would have occurred during melting and sintering. The off-stoichiometry of other elements was also detected, and the off-stoichiometry of Ni is especially noteworthy because Ni interstitial and vacancy/Ni antisites have been reported to affect the TEP of TiNiSn and ZrNiSn.[23–26] According to our EDS analysis, $Zr_{0.5}Ti_{0.5}NiSn_{0.98}Sb_{0.02}$ was deficient in Ni, and the other three samples had excess Ni, as shown in Table II.

Figure 5a shows the resistivity of the $Zr_xTi_{1-x}NiSn_{0.98}Sb_{0.02}$ samples measured by a ZEM-3 system, and the data for our $Hf_{0.25}Zr_{0.25}Ti_{0.5}NiSn_{0.98}Sb_{0.02}$ sample and $Zr_{0.5}Ti_{0.49}V_{0.01}NiSn_{0.98}Sb_{0.02}$ from a previous report[17] are also displayed for comparison. All the $Zr_xTi_{1-x}NiSn_{0.98}Sb_{0.02}$ samples have increasing resistivity with temperature, showing a metallic behavior, and the samples with higher Zr content ($x = 0.5, 0.75$) have lower resistivity. The resistivity of $Hf_{0.25}Zr_{0.25}Ti_{0.5}NiSn_{0.98}Sb_{0.02}$ was the highest across the whole temperature range,
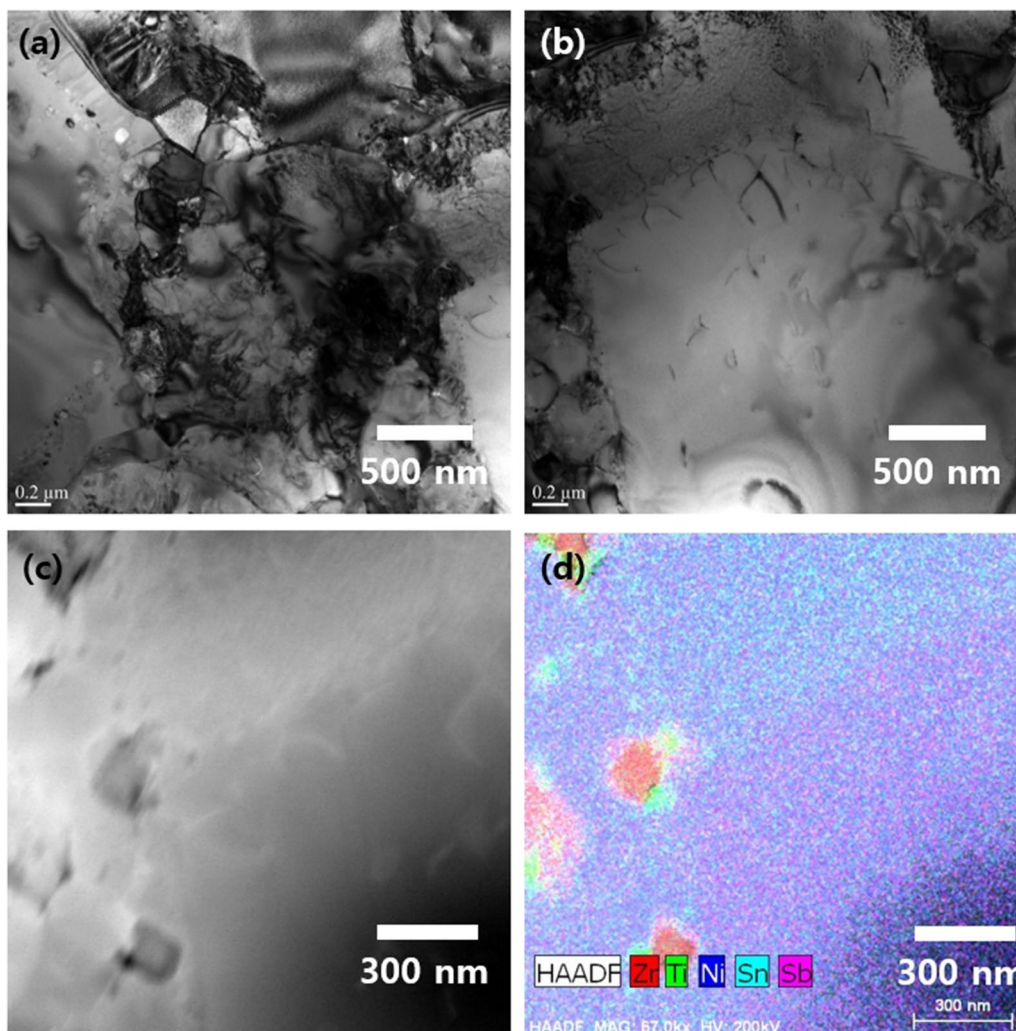

Fig. 4 (a), (b) and (c) show the TEM images for the $Zr_{0.75}Ti_{0.25}NiSn_{0.98}Sb_{0.02}$ sample, and (d) shows the elemental distribution maps by EDS analysis superposed on the image of (c).
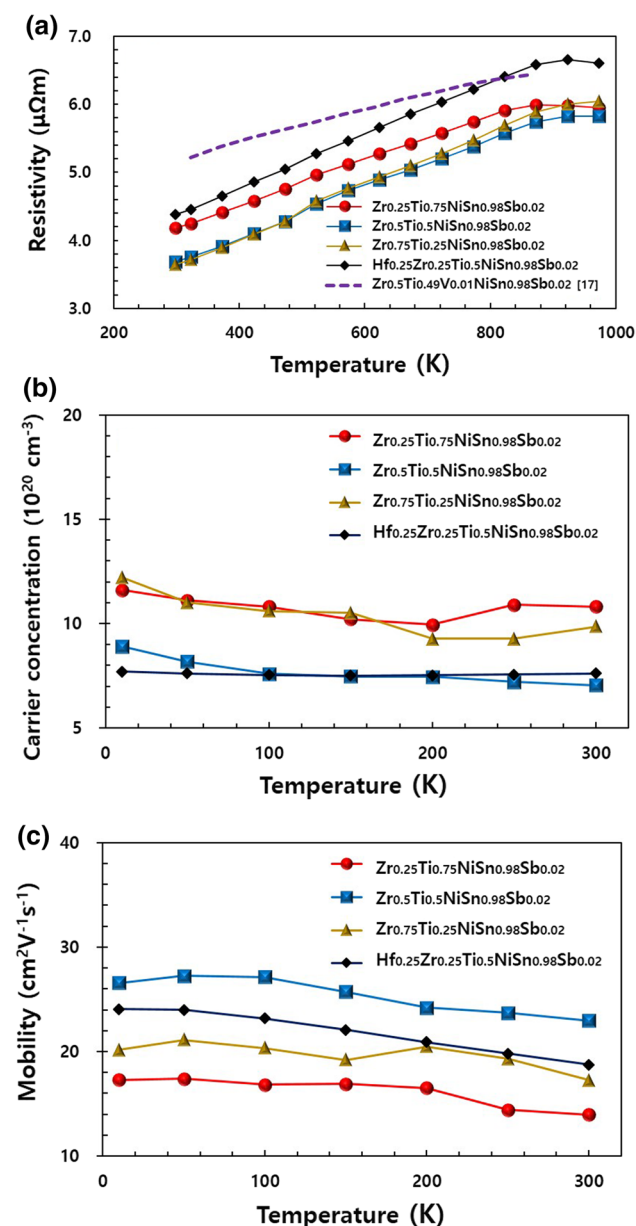
Fig. 5 Thermoelectric properties of the $Zr_xTi_{1-x}NiSn_{0.98}Sb_{0.02}$ (x = 0.25, 0.5, 0.75) and the $Hf_{0.25}Zr_{0.25}Ti_{0.5}NiSn_{0.9}8Sb_{0.02}$ versus temperature: (a) resistivity, (b) carrier concentration, and (c) carrier mobility.

Table I The lattice constants of the $Zr_xTi_{1-x}NiSn_{0.98}Sb_{0.02}$ samples determined by XRD analysis

Nominal composition	Average lattice constant (Å)	Deconvolution of the (220) peak
$Zr_{0.25}Ti_{0.75}NiSn_{0.98}Sb_{0.02}$	5.987	42.55°/42.68°
$Zr_{0.5}Ti_{0.5}NiSn_{0.98}Sb_{0.02}$	6.033	42.18°/42.35°
$Zr_{0.75}Ti_{0.25}NiSn_{0.98}Sb_{0.02}$	6.087	41.91°/42.11°

which is primarily due to the low carrier concentration, as shown in Fig. 5b. These PPMS data obtained by Hall measurements below 300 K show that the electron concentrations of $Hf_{0.25}Zr_{0.25}Ti_{0.5}NiSn_{0.98}Sb_{0.02}$ and $Zr_{0.5}Ti_{0.5}NiSn_{0.98}Sb_{0.02}$ are lower than 1×10^{21} cm^{-3}, whereas those of $Zr_xTi_{1-x}NiSn_{0.98}Sb_{0.02}$ samples (x = 0.25 and 0.75) are higher. Also, Fig. 5c compares the carrier mobility values, and it is noted that $Zr_{0.5}Ti_{0.5}NiSn_{0.98}Sb_{0.02}$ has the highest mobility, whereas $Zr_{0.25}Ti_{0.75}NiSn_{0.98}Sb_{0.02}$ shows the lowest values across the entire measurement temperature range.

According to previous studies, interstitial Ni (which would be closely related to excess Ni) was predicted to bring about shallow impurity bands in TiNiSn and ZrNiSn,[23,26] which also cause weak n-type doping and reduction of the carrier mobility in TiNiSn.[24] On the contrary, Ni deficiency was reported to increase carrier mobility.[25] These previous results seem to coincide with the data of Table II and Fig. 5, since the samples with Ni deficiency ($Zr_{0.5}Ti_{0.5}NiSn_{0.98}Sb_{0.02}$) has the lower concentration and highest mobility and vice versa. We think that the effects of Ni-related point defects on TEP are not negligible.

Figure 6a shows the Seebeck coefficients of the samples, and $Hf_{0.25}Zr_{0.25}Ti_{0.5}NiSn_{0.98}Sb_{0.02}$ has the highest negative thermopower of -161.1 µVK^{-1} at 873 K. Among the $Zr_xTi_{1-x}NiSn_{0.98}Sb_{0.02}$ samples, $Zr_{0.75}Ti_{0.25}NiSn_{0.98}Sb_{0.02}$ shows the highest negative peak value of -157.5 µVK^{-1} at 873 K. Next, Fig. 6b compares the power factor (PF) of the samples, which was calculated from the resistivity and the Seebeck coefficient according to the relation PF = S^2/ρ. It is noted that $Zr_{0.75}Ti_{0.25}NiSn_{0.98}Sb_{0.02}$ has the highest power factor of 4.31 mWm^{-1} K^{-2} at 823 K, while $Hf_{0.25}Zr_{0.25}Ti_{0.5}NiSn_{0.98}Sb_{0.02}$ has a plateau of about 4 mWm^{-1} K^{-2} over the temperature range of 573–873 K. $Zr_xTi_{1-x}NiSn_{0.98}Sb_{0.02}$ samples with x = 0.25 and 0.5 possess slightly lower PF$_{max}$ of 3.80 and 3.64 mWm^{-1} K^{-2}, respectively. Overall, Fig. 6b shows that the power factor of the Hf-free HH materials is comparable to the Hf-containing material in this study. However, Fig. 6c shows that there are significant gaps in the thermal conductivities. While the thermal conductivity of $Hf_{0.25}Zr_{0.25}Ti_{0.5}NiSn_{0.98}Sb_{0.02}$ does not exceed 4 Wm^{-1} K^{-1} across the entire temperature range, those of $Zr_xTi_{1-x}NiSn_{0.98}Sb_{0.02}$ samples are mostly in the range of 4–5 Wm^{-1} K^{-1}. Only the $Zr_{0.75}Ti_{0.25}NiSn_{0.98}Sb_{0.02}$ sample has values comparable to the Hf-containing sample at temperatures above about 720 K.

The thermal conductivity consists of three components: contribution by lattice (κ_{lat}), electron (κ_{el}), and bipolar conduction (κ_{bi}). Considering that our samples have very high majority carrier (electron) concentrations, as shown in Fig. 5b, the bipolar conduction component can be neglected, which results in the following relation:

Table II The measured composition of the HH samples by EDS analysis

Element	$Zr_{0.25}Ti_{0.75}NiSn_{0.98}Sb_{0.02}$		$Zr_{0.5}Ti_{0.5}NiSn_{0.98}Sb_{0.02}$		$Zr_{0.75}Ti_{0.25}NiSn_{0.98}Sb_{0.02}$		$Hf_{0.25}Zr_{0.25}Ti_{0.5}NiSn_{0.98}Sb_{0.02}$	
	at% (nominal)	at% (measured)	at% (nominal)	at% (measured)	at% (nominal)	at% (measured)	at% (nominal)	at% (measured)
Hf	–	–	–	–	–	–	8.34	8.49
Zr	8.34	7.00	16.67	16.45	25.00	25.53	8.34	8.29
Ti	25.00	29.43	16.67	20.26	8.34	9.28	16.66	17.41
Ni	33.33	34.25	33.33	32.26	33.33	33.45	33.33	33.95
Sn	32.67	29.01	32.67	30.76	32.67	31.53	32.67	31.51
Sb	0.66	0.31	0.66	0.26	0.66	0.21	0.66	0.34
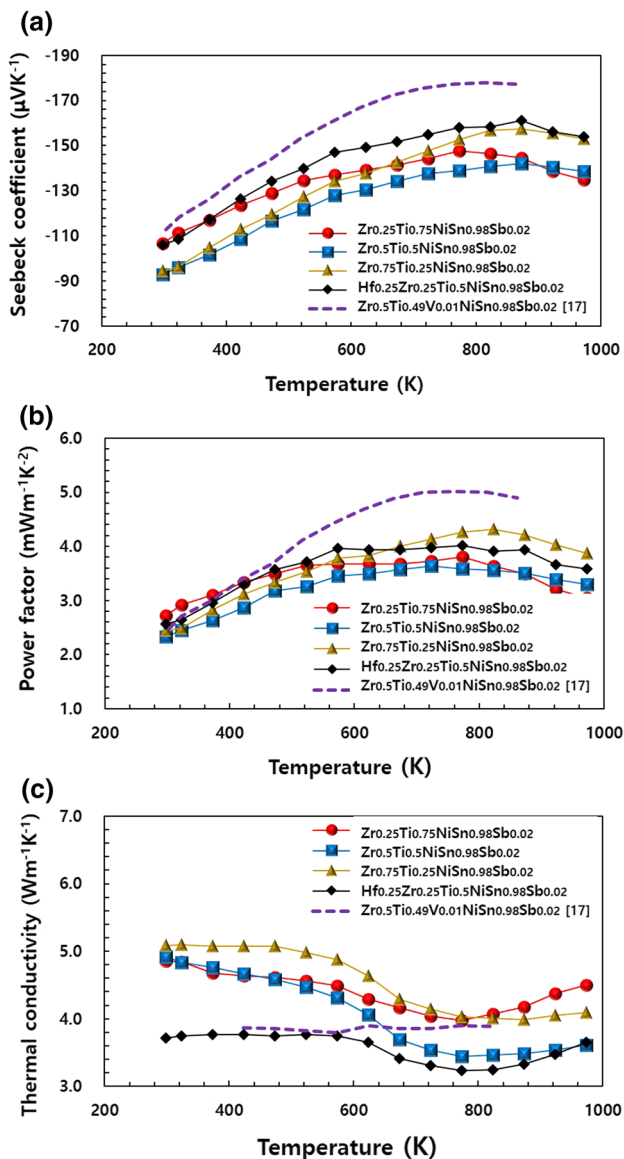
Fig. 6 Thermoelectric properties of the $Zr_xTi_{1-x}NiSn_{0.98}Sb_{0.02}$ ($x = 0.25$, 0.5, 0.75) and the $Hf_{0.25}Zr_{0.25}Ti_{0.5}NiSn_{0.98}Sb_{0.02}$ versus temperature: (a) Seebeck coefficient, (b) power factor, and (c) thermal conductivity.

$$\kappa = \kappa_{lat} + \kappa_{el}. \tag{1}$$

According to the Wiedemann–Franz law, the electron thermal conductivity κ_{el} is calculated from the Lorenz number (L), electrical conductivity, and temperature as follows:

$$\kappa_{el} = L\sigma T. \tag{2}$$

When the single parabolic band model is assumed, the Seebeck coefficient and the Lorenz number are calculated using Fermi–Dirac integrals $F_n(\xi)$:[27]

$$S = \pm\frac{k_B}{e}\left\{\frac{\left(r+\frac{5}{2}\right)F_{r+\frac{3}{2}}(\xi)}{(r+\frac{3}{2})F_{r+\frac{1}{2}}(\xi)} - \xi\right\} \tag{3}$$

$$L = \left(\frac{k_B}{e}\right)^2\left\{\frac{\left(r+\frac{7}{2}\right)F_{r+\frac{5}{2}}(\xi)}{(r+\frac{3}{2})F_{r+\frac{1}{2}}(\xi)} - \left[\frac{\left(r+\frac{5}{2}\right)F_{r+\frac{3}{2}}(\xi)}{\left(r+\frac{3}{2}\right)F_{r+\frac{1}{2}}(\xi)}\right]^2\right\} \tag{4}$$

$$F_n(\xi) = \int_0^\infty \frac{x^n}{1+e^{x-\xi}}dx \tag{5}$$

where r and ξ are the scattering parameter and the reduced Fermi energy E_F/kT, respectively. If we assume that the acoustic phonon scattering is dominant, r has a value of $-1/2$, and then ξ can be estimated from the experimental value of S by applying Eq. 3. Therefore, the Lorenz number L is calculated from Eqs. 4 and 5.

Figure 7a shows the calculated L of our samples. All the samples have L values in the range of 1.9×10^{-8}–2.1×10^{-8} WΩ K^{-2} at 298 K that decrease with temperature, and it is seen that $Hf_{0.25}Zr_{0.25}Ti_{0.5}NiSn_{0.98}Sb_{0.02}$ has the lowest value. Now κ_{el} is obtained by applying Eq. 2, by which κ_{lat} is also calculated. Figure 7b shows that κ_{el} monotonically increases with temperature, reaching the maximum values at 973 K. It is noted that κ_{el} of $Hf_{0.25}Zr_{0.25}Ti_{0.5}NiSn_{0.98}Sb_{0.02}$ is consistently the lowest, which is primarily due to the comparably low carrier

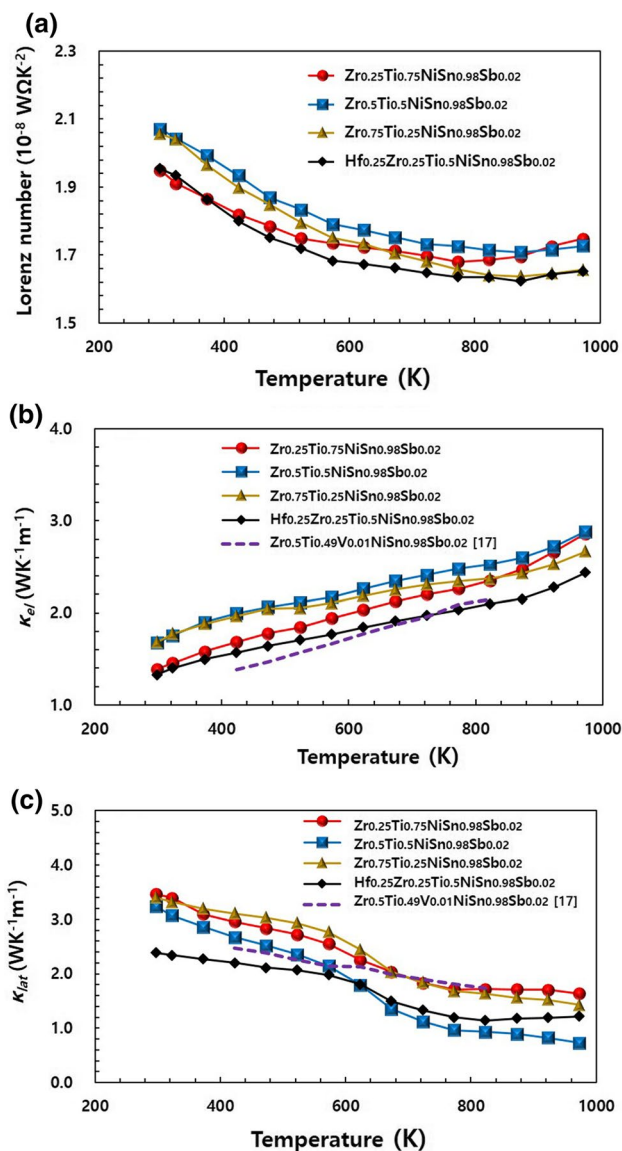**Fig. 8** Figures of merit for the $Zr_xTi_{1-x}NiSn_{0.98}Sb_{0.02}$ (x = 0.25, 0.5, 0.75) and the $Hf_{0.25}Zr_{0.25}Ti_{0.5}NiSn_{0.9}8Sb_{0.02}$ versus temperature.

Fig. 7 (a) Lorenz numbers, (b) electronic thermal conductivities, and (c) lattice thermal conductivities of the $Zr_xTi_{1-x}NiSn_{0.98}Sb_{0.02}$ (x = 0.25, 0.5, 0.75) and the $Hf_{0.25}Zr_{0.25}Ti_{0.5}NiSn_{0.9}8Sb_{0.02}$ versus temperature.

concentration as shown in Fig. 5b. Overall, κ_{el} of our Hf-free HH samples are considerably higher than the comparison data,[17] indicating that the carrier concentrations of our samples are higher than the optimum values for the maximum TEP.

Figure 7c compares the calculated values of κ_{lat} with temperature. As expected, the κ_{lat} of $Hf_{0.25}Zr_{0.25}Ti_{0.5}NiSn_{0.98}Sb_{0.02}$ is the lowest below about 600 K, but 600 K, the κ_{lat} of $Zr_{0.5}Ti_{0.5}NiSn_{0.98}Sb_{0.02}$ was lower than $Hf_{0.25}Zr_{0.25}Ti_{0.5}NiSn_{0.98}Sb_{0.02}$. In addition, with rising temperature, the κ_{lat} of the other Hf-free samples gradually decreases and becomes similar to that
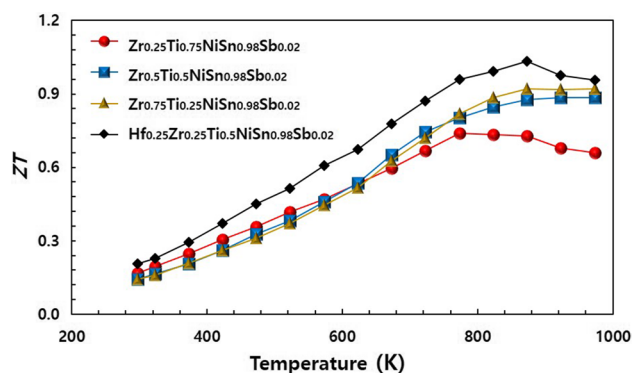
of Hf-containing samples. For now, the reason for this unexpected result is not clear, but the fact that vacancy/Ni antisites as well as interstitial Ni have been denoted as phonon scattering centers in TiNiSn[23] and ZrNiSn[28] leads us to assume that the Ni-related point defects are responsible for low κ_{lat} in our Hf-free samples. Otherwise, the Hf-containing material would have the lowest κ_{lat} across the measurement temperatures. The results of Fig. 7c may suggest that point defects related to Ni deficiency (which was confirmed in $Zr_{0.5}Ti_{0.5}NiSn_{0.98}Sb_{0.02}$) have a strong effect on the reduction of κ_{lat}.

Finally, Fig. 8 compares the ZT values of the samples. The highest ZT was obtained from $Hf_{0.25}Zr_{0.25}Ti_{0.5}NiSn_{0.98}Sb_{0.02}$ as a result of the lowest thermal conductivity, which was 1.03 at 873 K, while the Hf-free material with the best TEP was $Zr_{0.75}Ti_{0.25}NiSn_{0.98}Sb_{0.02}$ (ZT$_{max}$ = 0.92 at 873 K) in this study. The ZTs of $Zr_{0.5}Ti_{0.5}NiSn_{0.98}Sb_{0.02}$ were almost the same as those of $Zr_{0.75}Ti_{0.25}NiSn_{0.98}Sb_{0.02}$, while $Zr_{0.25}Ti_{0.75}NiSn_{0.98}Sb_{0.02}$ showed lower values (ZT$_{max}$ = 0.74 at 773 K). Detailed optimization of the Zr/Ti molar ratio as well as the carrier concentration may result in higher ZTs of $Zr_xTi_{1-x}NiSn$ HH materials.

Conclusions

Hf-free $Zr_xTi_{1-x}NiSn_{0.98}Sb_{0.02}$ HH materials with varied Zr/Ti molar ratios (x = 0.25, 0.5, 0.75) were fabricated using a conventional induction melting technique, ball milling, and SPS. The TEP was compared with the $Hf_{0.25}Zr_{0.25}Ti_{0.5}NiSn_{0.98}Sb_{0.02}$ sample processed by arc melting to estimate the effects of Hf alloying and melting method. The sintered $Zr_xTi_{1-x}NiSn_{0.98}Sb_{0.02}$ samples were nearly pure HH phases, but contained microscopic inclusions of unalloyed raw materials. In terms of TEP, the $Zr_xTi_{1-x}NiSn_{0.98}Sb_{0.02}$ HH materials had PFs comparable to those of the $Hf_{0.25}Zr_{0.25}Ti_{0.5}NiSn_{0.98}Sb_{0.02}$

sample, but the higher thermal conductivity of Hf-free HH limited the ZT_{max} to lower values. As a result, the ZT_{max} of Hf$_{0.25}$Zr$_{0.25}$Ti$_{0.5}$NiSn$_{0.98}$Sb$_{0.02}$ was about 12% higher ($ZT_{max} = 1.03$ at 873 K) than the best Hf-free Zr$_x$Ti$_{1-x}$NiSn$_{0.98}$Sb$_{0.02}$ HH material (0.92 in Zr$_{0.75}$Ti$_{0.25}$NiSn$_{0.98}$Sb$_{0.02}$ at 873 K). The possible contribution of Ni-related point defects to electronic and thermal transport properties was suggested. The adoption of a conventional induction melting technique instead of arc melting does not seem to have a critical impact on the final thermoelectric performance, which is a good sign for the development of a low-cost, scalable production process.

Conflict of interest The authors declare that they have no conflict of interest.

References

1. D. Champier, *Energy Convers Manag.* 140, 167 (2017).
2. L.E. Bell, *Science* 321, 1457 (2008).
3. S.B. Riffat, and X. Ma, *Appl. Therm. Eng.* 23, 913 (2003).
4. M. Gürth, G. Rogl, V.V. Romaka, A. Grytsiv, E. Bauer, and P. Rogl, *Acta Mater.* 104, 210 (2016).
5. G. Joshi, X. Yan, H. Wang, W. Liu, G. Chen, and Z. Ren, *Adv. Energy. Mater.* 1, 643 (2011).
6. M. Schwall, and B. Balke, *Phys. Chem. Chem. Phys.* 15, 1868 (2013).
7. T. Zhu, C. Fu, H. Xie, Y. Liu, and X. Zhao, *Adv. Energy Mater.* 5, 1500588 (2015).
8. A. Page, A. Van der Ven, P.F.P. Poudeu, and C. Uher, *J. Mater. Chem. A* 4, 13949 (2016).
9. W. Xie, A. Weidenkaff, X. Tang, Q. Zhang, J. Poon, and T.M. Tritt, *Nanomaterials* 2, 379 (2012).
10. F. Casper, T. Graf, S. Chadov, B. Balke, and C. Felser, *Semicond. Sci. Technol.* 27, 063001 (2012).
11. S. Ogut, and K.M. Rabe, *Phys. Rev. B* 51, 10443 (1995).
12. C. Uher, J. Yang, S. Hu, D.T. Morrelli, and G.P. Meisner, *Phys. Rev. B* 59, 8615 (1999).
13. L.D. Chen, X.Y. Huang, M. Zhou, X. Shi, and W.B. Zhang, *J. Appl. Phys.* 99, 064305 (2006).
14. G. Joshi, T. Dahal, S. Chen, H.Z. Wang, J. Shiomi, G. Chen, and Z. Ren, *Nano Energy* 2, 82 (2013).
15. O. Appel, M. Schwall, D. Mogilyansky, M. Kohne, B. Balke, and Y. Gelbstein, *J. Electron. Mater.* 42, 1340 (2013).
16. L. Chen, S. Gao, X. Zeng, A. Mehdizadeh Dehkordi, T.M. Tritt, and S.J. Poon, *Appl. Phys. Lett.* 107, 041902 (2015).
17. G. Rogl, P. Sauereschnig, Z. Rykavets, V.V. Romaka, P. Heinrich, B. Hinterleitner, A. Grytsiv, E. Bauer, and P. Rogl, *Acta Mater.* 131, 336 (2017).
18. S. Chen, K.C. Lukas, W. Liu, C.P. Opeil, G. Chen, and Z. Ren, *Adv. Energy Mater.* 3, 1210 (2013).
19. C. Yu, T.-J. Zhu, R.-Z. Shi, Y. Zhang, X.-B. Zhao, and J. He, *Acta Mater.* 57, 2757 (2009).
20. N.S. Chauhan, S. Bathula, A. Vishwakarma, R. Bhardwaj, B. Gahtori, A.K. Srivastava, M. Saravanan, and A. Dhar, *Materialia* 1, 168 (2018).
21. Y. Liu, H. Xie, C. Fu, G.J. Snyder, X. Zhao, and T. Zhu, *J. Mater. Chem. A* 3, 22716 (2015).
22. S. Populoh, M.H. Aguirre, O.C. Brunko, K. Galazka, Y. Lu, and A. Weidenkaff, *Scripta Mater.* 66, 1073 (2012).
23. H. Hazama, M. Matsubara, R. Asahi, and T. Takeuchi, *J. Appl. Phys.* 110, 063710 (2011).
24. S.A. Barczak, J. Buckman, R.I. Smith, A.R. Bakere, E. Don, I. Forbes, and J.-W.G. Bos, *Materials* 11, 536 (2018).
25. W. Ren, H. Zhu, J. Mao, L. You, S. Song, T. Tong, J. Bao, J. Luo, Z. Wang, and Z. Ren, *Adv. Electron. Mater.* 5, 1900166 (2019).
26. M. Schrade, K. Bereland, A. Kosinskiy, J.P. Heremans, and T.G. Finstad, *J. Appl. Phys.* 127, 045103 (2020).
27. H.J. Goldsmid, *Introduction to Thermoelectricity* (Berlin: Springer, 2010), pp. 23–41.
28. A. Katre, J. Carrete, and N. Mingo, *J. Mater. Chem. A* 4, 15940 (2016).

Publisher's Note Springer Nature remains neutral with regard to jurisdictional claims in published maps and institutional affiliations.